Open Access Articles

Rates and kinematics of active shortening along the eastern Qilian Shan, China, inferred from deformed fluvial terraces

The Faculty of Oregon State University has made this article openly available.
Please share how this access benefits you. Your story matters.

Citation	Hu, X., Pan, B., Kirby, E., Gao, H., Hu, Z., Cao, B., ... & Zhang, G. (2015). Rates and kinematics of active shortening along the eastern Qilian Shan, China, inferred from deformed fluvial terraces. Tectonics, 34(12), 2478-2493. doi:10.1002/2015TC003978
DOI	10.1002/2015TC003978
Publisher	John Wiley & Sons, Inc.
Version	Version of Record
Terms of Use	http://cdss.library.oregonstate.edu/sa-termsofuse

AGU PUBLICATIONS

Tectonics

RESEARCH ARTICLE
10.1002/2015TC003978

Key Points:
- Fluvial terraces are deformed across the range front of the eastern Qilian Shan
- Terrace deformation constrains fault geometry and displacement
- Chronology of terrace deposits constrains slip rates of ~1 mm/yr

Correspondence to:
X. Hu,
feixhu@lzu.edu.cn

Citation:
Hu, X., B. Pan, E. Kirby, H. Gao, Z. Hu, B. Cao, H. Geng, Q. Li, and G. Zhang (2015), Rates and kinematics of active shortening along the eastern Qilian Shan, China, inferred from deformed fluvial terraces, *Tectonics*, *34*, 2478–2493, doi:10.1002/2015TC003978.

Received 28 JUL 2015
Accepted 12 NOV 2015
Accepted article online 14 NOV 2015
Published online 17 DEC 2015

©2015. American Geophysical Union. All Rights Reserved.

Rates and kinematics of active shortening along the eastern Qilian Shan, China, inferred from deformed fluvial terraces

Xiaofei Hu[1], Baotian Pan[1], Eric Kirby[2], Hongshan Gao[1], Zhenbo Hu[1], Bo Cao[1], Haopeng Geng[1], Qingyang Li[1], and Guoliang Zhang[1]

[1]Key Laboratory of Western China's Environmental Systems (Ministry of Education), College of Earth and Environmental Sciences, Lanzhou University, Lanzhou, China, [2]College of Earth, Ocean, and Atmosphere Science, Oregon State University, Corvallis, Oregon, USA

Abstract In the eastern Qilian Shan, a flight of fluvial terraces developed along the Jinta River valley are deformed across the Nanying anticline. Four individual fluvial terraces are preserved at different elevations above the river, and higher terrace treads are draped by systematically thicker aeolian loess. Optically stimulated luminescence dating of deposits at the base of the loess provides constraints on the timing of surface abandonment; terraces were abandoned at 69 ± 4 ka B.P. (T4), 57 ± 4 ka B.P. (T3), and between 34 ± 3 ka B.P. (T2), respectively. Differential GPS measurement of the terrace profile across the anticline allows reconstruction of subsurface fault geometry; we model terrace deformation above a listric thrust fault with a tip line at 2.2 ± 0.1 km depth and whose dip shallows systematically to 23 ± 3° at depth of 5.8 ± 1.1 km. Combining terrace ages with this model of fault geometry, we estimate a shortening rate of 0.8 ± 0.2 mm/a across the Nanying fold and a shortening rate of ~0.1 mm/a across the mountain front fault since ~70 ka B.P. This rate suggests that the frontal fault system along the eastern Qilian Shan accomplishes crustal shortening at rates of approximately 0.9 ± 0.3 mm/a during late Pleistocene time.

1. Introduction

Various simple geometric models of fault-related folds (fault-bend fold, fault-propagation fold, detachment fold, and trishear fold) have been proposed to explain shortening and deformation of upper crust in regions of active mountain building [*Allmendinger*, 1998; *Erslev*, 1991; *Hardy and Poblet*, 1994; *Suppe*, 1983; *Suppe and Medwedeff*, 1990; *Wickham*, 1995]. Collectively, these studies utilize both preexisting strata [*Burchfiel et al.*, 1999; *Chen et al.*, 2007; *Daëron et al.*, 2007; *Hubert-Ferrari et al.*, 2007; *Molnar et al.*, 1994], syntectonic or "growth" strata [*Storti and Poblet*, 1997; *Suppe*, 1992], and geomorphic markers [*Benedetti et al.*, 2000; *Lavé and Avouac*, 2000; *Rockwell et al.*, 1988; *Thompson et al.*, 2002; *Wilson et al.*, 2009] to reconstruct the kinematics of fold/fault growth. Fluvial terraces, in particular, can be particularly useful along the margins of active mountain ranges, where the absence of sediment accumulation does not provide a stratigraphic record of fault growth. Where flights of fluvial terraces are to be preserved across fold hinges [e.g., *Lavé and Avouac*, 2000; *Thompson et al.*, 2002; *Gold et al.*, 2006; *Scharer et al.*, 2006; *Daëron et al.*, 2007; *Wilson et al.*, 2009], the geometry of deformation can place constraints on the subsurface geometry and kinematics of fault slip [*Thompson et al.*, 2002; *Scharer et al.*, 2006]. Of course, one of the critical challenges in exploiting fluvial terraces is establishing a robust chronology of terrace formation and abandonment [e.g., *Lavé and Avouac*, 2000].

Cenozoic mountain building along the northern margin of the Himalayan-Tibetan orogen has led to the growth of the Qilian Shan along a series of thrust faults that appear to root into a midcrustal décollement [*Burchfiel et al.*, 1989; *Tapponnier et al.*, 1990; *Meyer et al.*, 1998]. Along portions of the range, Cenozoic shortening [*Fang et al.*, 2005; *Geoge et al.*, 2001; *Liu et al.*, 2011; *Zheng et al.*, 2010] has been accommodated along reactivated structures that first developed during the Early Paleozoic [*Yang et al.*, 2007]. At present, active deformation is largely accomplished by displacement along a system of northeast vergent thrust faults [*Hetzel et al.*, 2004, 2006; *Hetzel*, 2013; *Palumbo et al.*, 2009; *Champagnac et al.*, 2010; *Zheng et al.*, 2010] at the northern foot of the range (North Frontal Thrusts, NFT) and define the border between the range and the sedimentary basins of the Hexi Corridor (Figure 1). The range is composed of deformed Precambrian-Paleozoic strata and Early Paleozoic granitoid plutons; Neogene strata are preserved sporadically along the mountain front [*Gansu Geological Bureau*, 1989]. Within the eastern Qilian Shan (Figure 2), flights of late Quaternary fluvial terraces are well preserved across the NFT. Moreover, a robust chronology exists for these

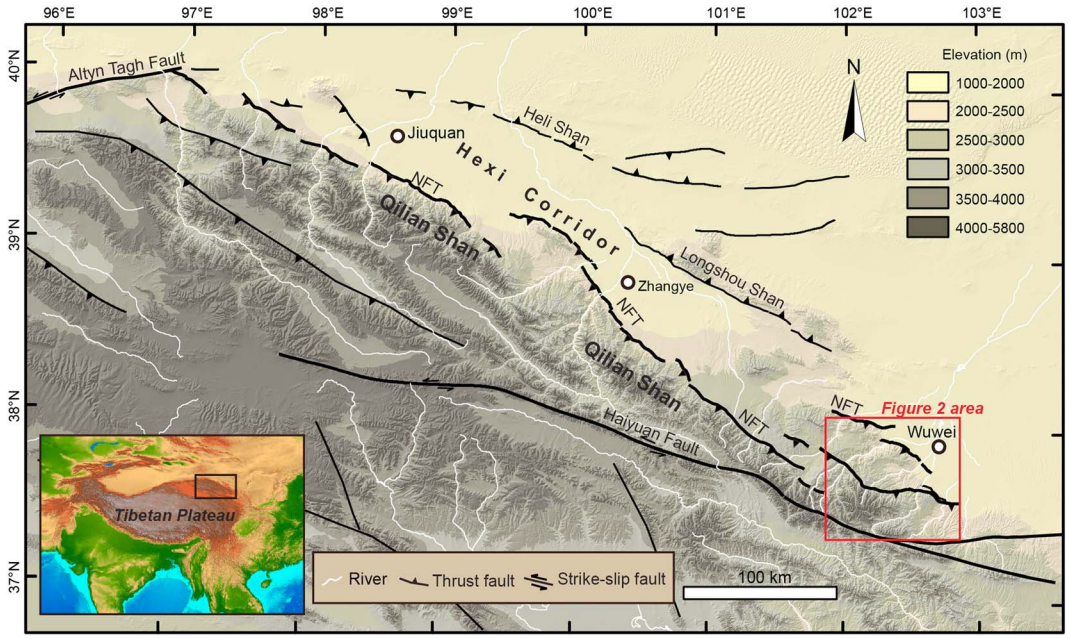

Figure 1. Topographic map of the Qilian Shan derived from SRTM (Shuttle Radar Topography Mission) image. The southwest dipping fault NFT (North Frontal Thrust of the Qilian Shan) separates the Qilian Shan mountain range from the Hexi Corridor in the north. In the eastern Qilian Shan, near the city Wuwei, the NFT bifurcates into two major faults in separating different mountain ranges of the Qilian Shan. Active fault locations are shown following *Meyer et al.* [1998], *Hetzel et al.* [2002, 2004, 2006], *Yuan et al.* [2013], *Zheng et al.* [2013a, 2013c], and our own observations.

terraces that relies on a combination of magnetostratigraphy and optically stimulated luminescence (OSL) dating of aeolian loess that overlies terrace gravels [*Pan et al.*, 2007, 2013]. This combination of laterally extensive, well-dated fluvial terraces provides an opportunity to place constraints on the geometry and displacement rates along the NFT.

In this study, we utilize a flight of late Pleistocene fluvial terraces along the Jinta River to answer several questions regarding the NFT: What is the geometry of active faults beneath the folded surface along the eastern Qilian Shan? What are the kinematics and rate of fault slip and fold growth during the late Quaternary? How does slip along the NFT contribute to rock uplift and growth of the Qilian Shan?

2. Study Area

2.1. Geologic Setting

The ranges of the eastern Qilian Shan near the city of Wuwei (Figure 2) are composed of Early Paleozoic plutonic rocks, including granite, granodiorite, and plagiogranite, which intrude deformed Paleozoic metasedimentary rocks [*Gansu Geological Bureau*, 1989] (Figure 2b). Although deformation during the late Cenozoic appears to have been controlled by the NFT thrust system [*Gaudemer et al.*, 1995], unconformities between both Jurassic and Neogene terrestrial sedimentary rocks [*Gansu Geological Bureau*, 1989] suggest the likelihood of Mesozoic and/or early Cenozoic deformation. Red sandstones of Neogene age rest unconformably on older rocks and are not coincident with pre-Cenozoic depocenters, suggesting some deformation prior to the Cenozoic. Dipping Neogene sandstones are buried by Quaternary fluvial gravels and aeolian loess along the mountain front and up river valleys into the range. Loess deposition on low-relief surfaces, both bedrock and fluvial terraces, reaches thicknesses of ~100 m, and the earliest loess deposition in this region is dated to 1.41 Ma B.P. [*Pan et al.*, 2007].

2.2. Active Tectonics

Along the mountain crest, the eastern segment of the Haiyuan Fault, the Lenglongling Fault (Figure 1), bifurcates into the Gulang Fault to the east and the Laohushan-Maomaoshan Fault to the southeast (Figure 1). This fault system has been active during the late Cenozoic and Quaternary as a left-lateral strike-slip

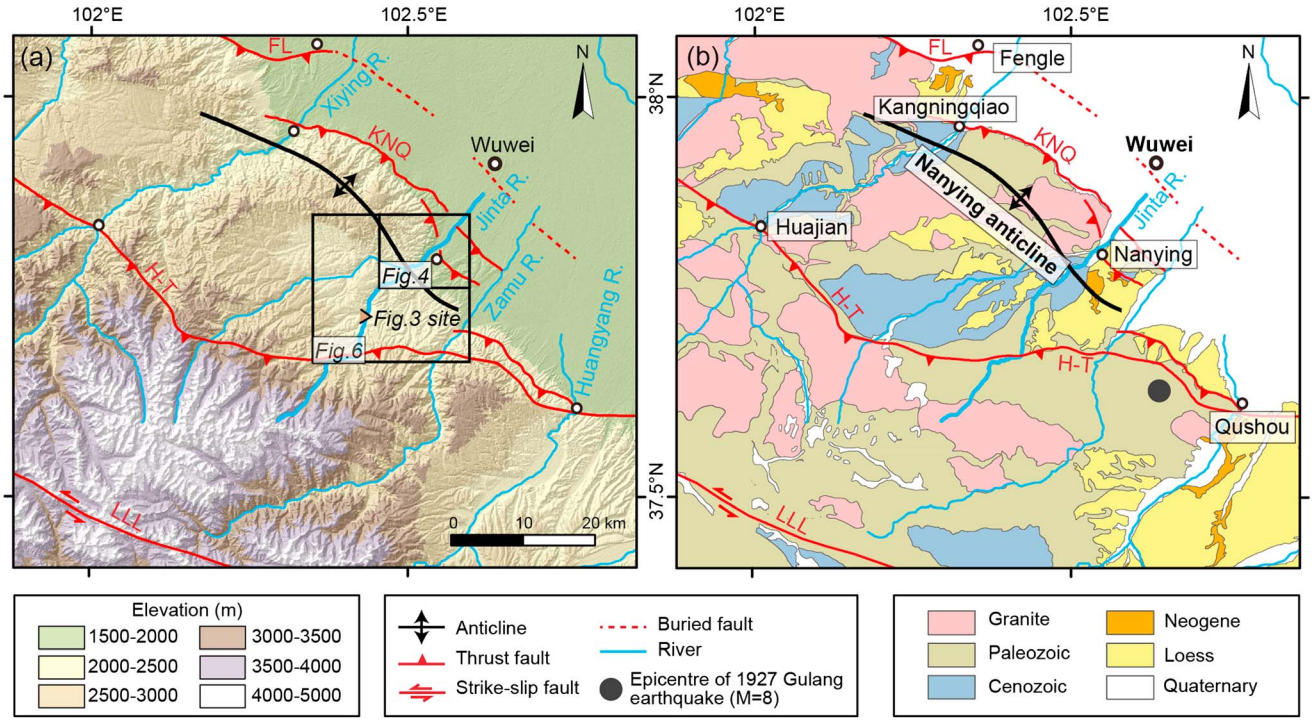

Figure 2. (a) Color shaded digital elevation model of the eastern Qilian Shan derived from SRTM (Shuttle Radar Topography Mission) image. (b) Simplified geologic map showing the distribution of bedrock lithology [*Gansu Geological Bureau*, 1989] and active faults. FL: the Fengle fault; KNQ: the Kangningqiao fault; H-T: the Huangcheng-Taerzhuang fault; and LLL: the Lenglongling Fault.

fault [*Gaudemer et al.*, 1995; *Lasserre et al.*, 2002]. To the north, NE vergent thrust faults (Figure 2) of the NFT system constitute the primary active faults along the eastern Qilian Shan. The northernmost branch of the fault system is locally named the Fengle fault (Figure 2), which offsets Quaternary alluvial fans and terrace surface along the Dongda River near Fengle. To the southwest of Fengle (Figure 2a), *Champagnac et al.* [2010] used cosmogenic exposure dating to obtain a relatively high throw rate of 2.8 ± 1.8 mm/a since 30 ka B.P. Toward the east, however, the Fengle fault tip becomes blind near or south of the city of Wuwei (Figure 2) [*Gaudemer et al.*, 1995]. The mountain front steps to the south at this point, and the range front is defined by a fault extending from Kangningqiao to just north of Nanying (Figure 2); this fault is referred to as the Kangningqiao fault (KNQ) (but was referred to as the Shiyang Thrust by *Gaudemer et al.* [1995]). Farther east, the mountain front again steps southward and is bound by the Huangcheng-Taerzhuang fault (H-T), which extends from the town of Huangchen in the west, through the Xiying River near Huajian, and terminates at the Huangyang River near Qushou (Figure 2b). The 1927, $M = 8.3$, Gulang earthquake occurred along the H-T fault [*Gaudemer et al.*, 1995; *Hou*, 1998], and a slip rate determined along the eastern segment of this fault yielded a vertical component of 0.54–0.80 mm/yr during the Holocene time [*Chen*, 2003]. Although the general framework of active deformation is reasonably well known [*Gaudemer et al.*, 1995], the detailed kinematics and slip rate of the thrust system along the eastern Qilian Shan remain poorly studied. In particular, there are no existing slip rate estimates from the Kangningqiao fault (Figure 2).

2.3. Geomorphic Evolution

The mountain crest of the eastern Qilian Shan has an elevation of ~5000 m, and the relief decreases from the crest to the Hexi Corridor at an elevation of 1500–1700 m (Figure 2). Separated by the H-T fault system, the ranges can be clearly separated into two regions with respect to landscape relief. South of the H-T thrust, peak elevations range from 3700 to 5000 m, whereas north of the H-T thrust, the range has elevations of 2500–3200 m (Figure 2). Along the divides of the drainage basins, remnants of low-relief planation surfaces with gentle slope are identified [*Gaudemer et al.*, 1995; *Pan et al.*, 2007]. Although no definite age control exists for when this surface developed in the eastern Qilian Shan, it may be comparable with the planation surface in Hoh Xil area, which has been suggested to have developed prior to 7.0–3.6 Ma B.P. [*Pan et al.*, 2004]. This old

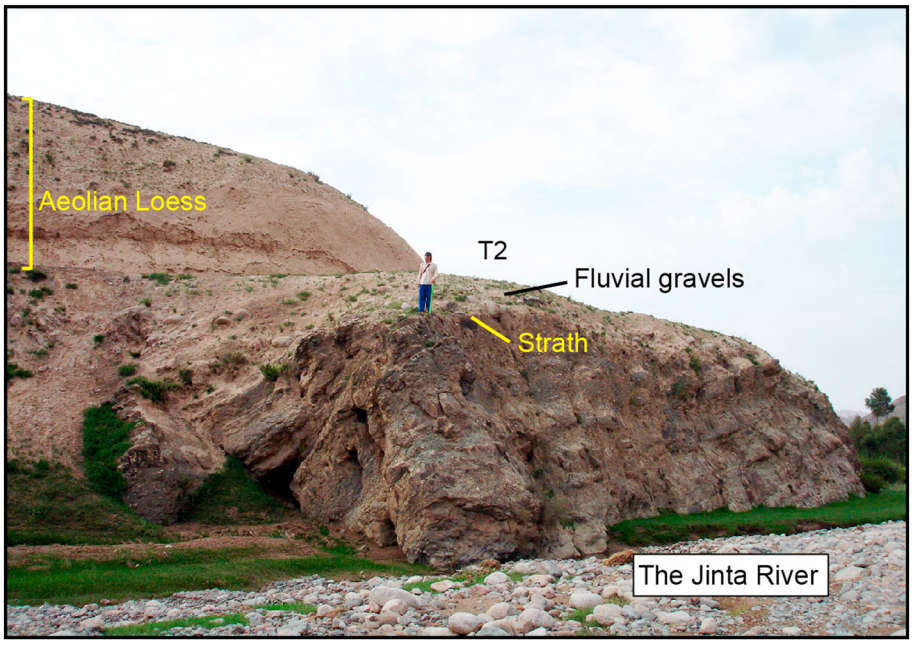

Figure 3. The Photo showing the lithology of a strath terrace (T2) developed in Paleozoic metasedimentary rocks along the Jinta River. The strath surface is capped by a 1–5 m layer of fluvial gravel and 15–20 m aeolian loess.

surface is strongly deformed by the thrust and fold related to the movement on the basement ramps [*Gaudemer et al.*, 1995]. In the basin of the Jinta River, an intermediate surface between the planation surface and modern river valley with an elevation of 2200–2700 m has been suggested to have formed prior to 1.4 Ma B.P. based on magnetostratigraphy of overlying loess [*Pan et al.*, 2007]. Below this erosion surface, flights of fluvial terraces are developed along the modern drainage system. The oldest terraces along river valleys are dated by magnetostratigraphy of overlying loess [*Pan et al.*, 2003] and electron spin resonance (ESR) dating; collectively, these suggest ages of 0.8–1.2 Ma B.P. [*Pan et al.*, 2007]. Differences in the height of these terraces along the river, however, suggest differential uplift between high mountain range to the south and the low mountain range farther north [*Pan et al.*, 2013]. This relative incision pattern appears to be influenced by the frontal fault system, and to better constrain the geometry and the slip rate of these structures, we focused the study of the fluvial terrace sequences.

3. Fluvial Terraces Along the Jinta River

Flights of Pleistocene fluvial terraces are exceptionally well developed along the Jinta River (Figure 2) and are well preserved along almost the entire river reach. Most of the Pleistocene terraces are strath terraces that are capped by 1–5 m of fluvial gravels, which are subsequently buried by variable depths of aeolian loess (Figure 3). In this area, aeolian loess deposition began approximately 1.4 Ma B.P. [*Wang et al.*, 2007], and cyclic loess-paleosol sequences [*Wang et al.*, 2007; *Wu et al.*, 2001] suggest a continuous history of loess deposition. This sequence can be exploited to provide constraints on the abandonment of terrace treads [*Pan et al.*, 2013]. In order to characterize active deformation, our investigation mainly focuses on young terraces (late Pleistocene terraces). There are two advantages with young terraces: The first is they are often preserved along long reaches of the river allowing for more precise correlation. Second, they are accessible to dating via OSL in the overlying loess. Our chronology for this study partly relies on previous dating of terraces along the Jinta River [*Pan et al.*, 2007, 2013], to which we add additional data. Differential GPS was used to measure the terrace height; elevations are precise to within ~10 cm. Because the gravel tread is clearly visible beneath the loess cover, our terrace height data are surveyed on the top of the fluvial gravel layers, as discussed by *Pan et al.* [2013], because the gravels are thin relative to the height of the terrace (Figures 3, 5, and 6) and this introduces only minor variations in elevation into our data (Figure 8).

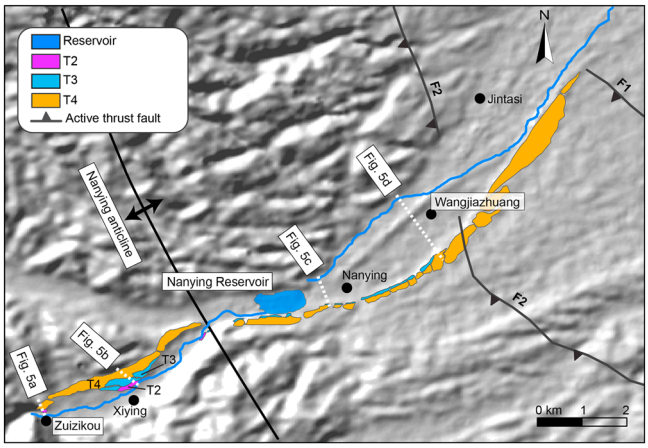

Figure 4. Map of the distribution of fluvial terraces along the Jinta River based on field work. The background is a shaded relief image. Dashed lines in white are cross sections of the river valley showing terrace levels in Figure 5. Two faults F1 and F2 are coincident with the mountain front.

3.1. Terrace Distribution

Along the Jinta River, at least six individual fluvial terrace levels are preserved [*Pan et al.*, 2007, 2013]. Based on ESR (electron spin resonance) dating, the highest terrace appears to have formed around 1.2 Ma B.P. [*Pan et al.*, 2007]. Two late Pleistocene terraces were dated by OSL at 72.8 ± 7.2 ka (T4 in this study according to terrace correlation) and 56.1 ± 3.5 ka (T3 in this study according to terrace correlation), respectively [*Pan et al.*, 2007]. In recent study [*Pan et al.*, 2013], T4 was dated as 71.0 ± 6.3 ka and T2 was dated as 37.4 ± 4.7 ka using OSL method. In this study, we focus on the three levels of late Pleistocene terraces (T4, T3, and T2) [see *Pan et al.*, 2013], which are widely distributed in the reach from H-T fault to Nanying (Figure 2). Downstream of Nanying (Figure 4), terrace preservation is sparse, and only T4 is preserved near the KNQ fault (F1 and F2 in Figure 4). In the upper reach of the Jinta River, the river valley is usually narrow, and the preserved terraces are also quite narrow. Below Zuzikou, however, the river valley becomes wider, and the terrace surfaces become correspondingly broader (Figure 4). Of these late Pleistocene terraces, T4 is the most continuous surface (Figure 4). Although T3 is not so widely distributed as T4, it can be found continuously along the river from Xiwan to the area of Nanying. T2 is largely preserved only in the upper reach, above the Nanying reservoir, and is missing or not developed in the downstream reach (Figure 4).

3.2. Terrace Staircases

In the Jinta River valley, four transects (Figures 4 and 5) are illustrated here to show the characteristics of the late Pleistocene terraces. Along the Zuizikou transect (Figure 5a), two late Pleistocene terraces (T4 and T2) and one Holocene terrace (T1) are developed. These are all strath terraces where the bedrock surface is covered by a thin layer of rounded cobbles and boulders. The river valley is relatively narrow in this reach, and the T4 and T2 are preserved in both sides of the valley. On the north side of the river, the terrace surface is broader than the south, so thicker aeolian loess is preserved on top of the fluvial sediment (Figure 5a). The depth of the T4 fluvial sediment is 1–2 m, and the top of the depositional surface is 41.2 m high above the modern river level. Atop this, approximately 10–20 m of aeolian loess has accumulated. T2 has a similar structure with T4 (Figure 5a), and the height of the fluvial sediment is 13.4 m above the modern river level.

Along the Xiwan transect (Figures 4 and 5b), the river valley is broader and each late Pleistocene terrace has a somewhat wider surface (Figure 5b). Detailed terrace descriptions can be found in *Pan et al.* [2013]. In this site, we collected one additional sample on T3 for dating by the OSL method, which was lacking in the previous study [*Pan et al.*, 2013].

Below the Nanying reservoir, two late Pleistocene terraces (T3 and T4) are developed at the Nanying section (Figure 5c), but the T2 surface is missing. The top of the T4 fluvial sediment is 34.2 m above the modern rive level, and its top is capped by 30–40 m aeolian loess. T3 is preserved as a narrow band (Figure 5c), less than 100 m wide, and has more than 3 m of fluvial gravel atop the strath. The top of the fluvial sediment is 26 m and capped by 15–25 m aeolian loess.

At the Wangjiazhuang transect (Figure 5d), only the T4 terrace is present today. Above the T4 strath, about 4 m fluvial sediment (cobbles and boulders) was deposited, and the top of the fluvial sediment is 17.8 m above the modern river level. The fluvial sediment is capped by 20–30 m aeolian loess.

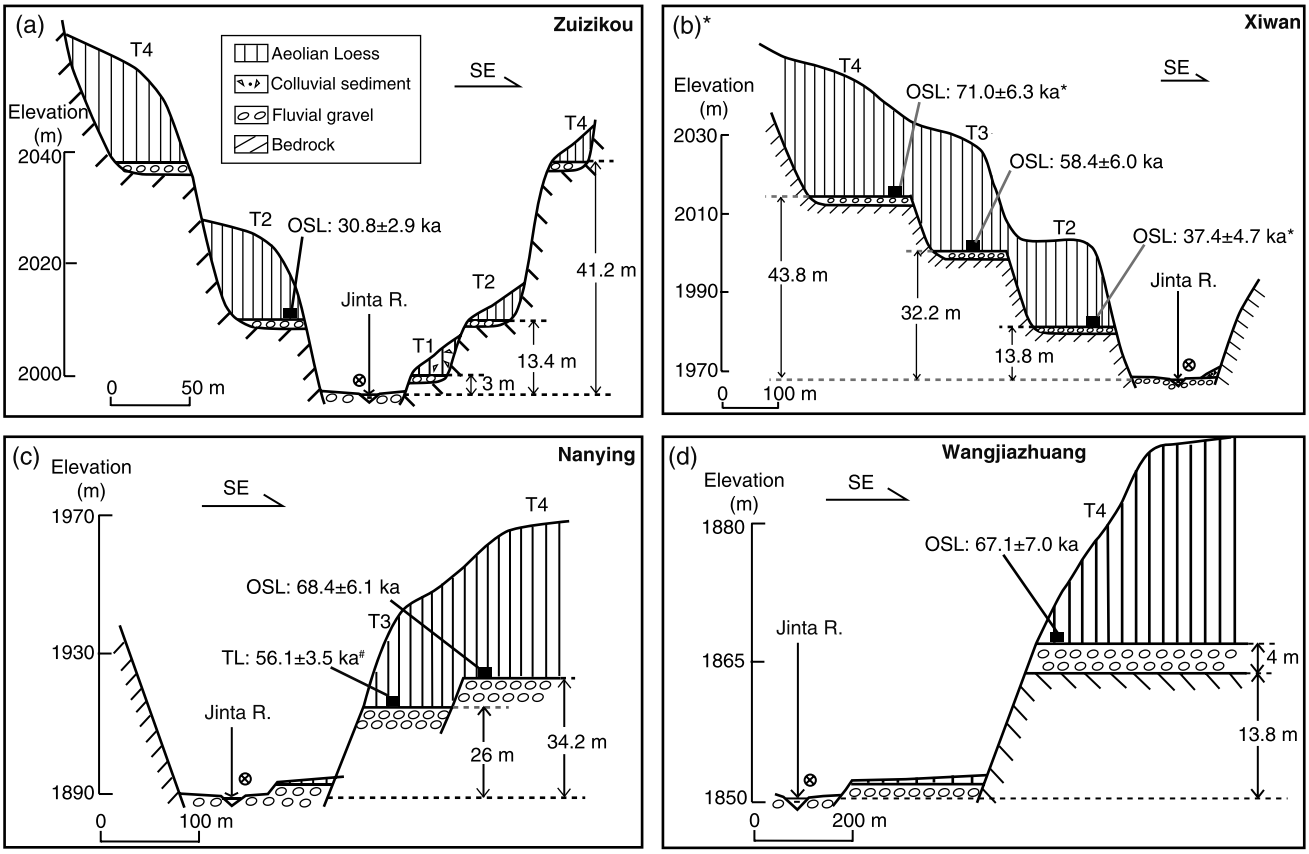

Figure 5. Four cross sections of the Jinta River valley showing late Pleistocene terraces. (a) Zuizikou transect: Three strath terraces (T1, T2, and T4) are developed, and T3 is missing in this area. The bedrock of the terraces is composed of Cenozoic sedimentary rocks. (b) Xiwan transect (the graph, T2, and T4 OSL ages are referenced to *Pan et al.* [2013]): Three strath terraces (T2–T4) are developed on Cenozoic sedimentary rocks, and T1 is missing in this area. (c) Nanying transect: Only two terraces (T3 and T4) are developed. The TL data are referenced to *Pan et al.* [2007]. (d) Wangjiazhuang transection: Only one strath terrace T4 is developed in this area. The bedrock of the terrace is Neogene sedimentary rocks.

3.3. New Terrace Ages

Late Pleistocene aeolian loess is one of the more reliable deposits for OSL dating as long-duration exposure to sunlight ensures complete bleaching [*Aitken*, 1998]. We develop bounding ages on the abandonment of terrace surfaces by dating the lowermost aeolian loess deposited atop the fluvial gravels on terrace treads [*Pan et al.*, 2003, 2007, 2013]. In previous terrace studies [*Pan et al.*, 2003, 2007, 2013] in this region, the validation of overlying loess control on the terrace abandonment time was well discussed [e.g., *Pan et al.*, 2013], and in at least one study near Lanzhou where both fluvial gravels and overlying loess were dated independently [*Hu et al.*, 2011], it can be demonstrated that loess accumulation is close in time to abandonment of the terrace treads. Thus, in this study we also use the OSL dating of the lowermost loess to control the minimum age for the terrace abandonment. With the previous results, we add four new dates for the late Pleistocene terraces along the Jinta River (Table 1). OSL samples were collected in stainless steel cubes, hammered into a face at least 30 cm deep from the previously exposed outcrop surface (Figure 6). In the OSL Chronology Lab (Key Laboratory of Western China's Environmental Systems, Ministry of Education, Lanzhou University), quartz grains of 38–63 μm for pure aeolian loess samples and quartz grains of 90–125 μm for mixed aeolian-alluvial samples were extracted and purified to follow the process of *Fan et al.* [2010]. The distribution of D_e values for each sample is concentrated as supported by the radial plot of representative sample 080404 (Figure 7). The analysis of D_e and calculation of OSL ages are following *Fan et al.* [2015]. Sample information and measurement results are presented in Table 1. For clarity, we also include three other luminescence samples from previous studies that we rely on for our chronology of terrace abandonment.

Table 1. Luminescence Sample Information and Analysis Data[a]

Sample Number	Terrace	Material	Height Above Gravels (m)	Longitude (°E)	Latitude (°N)	Altitude (m)	U (ppm)	Th (ppm)	K (ppm)	Equivalent Dose (Gy)[b]	Dose Rate (mGy/a)	Cosmic Ray Rate (Gy/ka)	Aliquot	Age[c] (ka)	Reference
080404	T4	Loess	0.3	102.525	37.792	1901	3.38	11.3	1.81	227.0 ± 14.5	3.32 ± 0.21	0.041	8	68.4 ± 6.1	This study
080403	T4	Loess	0.4	102.547	37.803	1844	2.94	10.8	2.05	233.8 ± 9.0	3.49 ± 0.34	0.064	7	67.1 ± 7.0	This study
(1)	T4			102.475	37.774	2036								70.1 ± 6.3	*Pan et al.* [2013]
NYH0705-02	T3	Loess	0.6	102.481	37.776	2013	3.49	12.3	2.06	201.9 ± 6.7	3.46 ± 0.34	0.029	14	58.4 ± 6.0	This study
(2)	T3				Nanying									56.1 ± 3.5	*Pan et al.* [2007]
072805	T2	Loess mixed with sands	0.3	102.474	37.771	1993	2.95	10.1	2.56	98.4 ± 6.8	3.19 ± 0.20	0.067	16	30.8 ± 2.9	This study
(3)	T2			102.484	37.781	1983								37.4 ± 4.7	*Pan et al.* [2013]

[a]Uncertainties in equivalent dose, dose rate, and age represent 1σ. Analysis and measurement are completed in OSL Chronology Lab, Key Laboratory of Western China's Environmental Systems, Ministry of Education, Lanzhou University, China.
[b]Equivalent dose (D_e) was measured using modified single-aliquot regenerative dose protocol [*Banerjee et al.*, 2001] for quartz (see details of the protocol in *Fan et al.* [2015]).
[c]The D_e values are calculated based on central age model, because D_e values of each sample are concentrated (Figure 7).

On the T4 terrace, *Pan et al.* [2007] had determined an age of 72.8 ± 7.2 ka using infrared stimulated luminescence from the basal loess overlying T4 terrace gravels (T3 in the study of *Pan et al.* [2007]). We redated this terrace at the Nanying section (Figures 4 and 5c), and our data suggest an OSL age of 68.4 ± 6.1 ka (Figure 5c and Table 1, number 080404), consistent within uncertainty. There are two additional age determinations from the T4 terrace: 71.0 ± 6.3 ka [*Pan et al.*, 2013] at the Xiwan section (Figure 5b) and 67.1 ± 7.0 ka (Table 1, number 080403) at Wangjiazhuang section (Figure 5d). These ages are all obtained from the base of loess overlying T4, and their relatively good agreement suggests that the abandonment of the T4 terrace occurred before 67–73 ka, giving a weighted mean age of 69 ± 4 ka (representing 1σ uncertainty).

For the T3 terrace tread, we obtained a new OSL age from the basal loess overlying T3 at Xiwan section (Figures 5b and 6). Our results yield an age of 58.4 ± 6.0 ka (Table 1, number NYH0705-02), which is again consistent with the previously determined thermoluminescence (TL) age of 56.1 ± 3.5 ka [*Pan et al.*, 2007] at the Nanying section (Figure 5c). These two ages on T3 indicate that the abandonment time for T3 surface occurred before 52–60 ka, giving a weighted mean age of 57 ± 4 ka (representing 1σ uncertainty).

Finally, for the T2 terrace, previous work at the Xiwan section (Figure 5b) yielded an OSL age of 37.4 ± 4.7 ka [*Pan et al.*, 2013]. For the same flight of T2 at the Zuzikou section (Figure 5a), our results yield an age of 30.8 ± 2.9 ka (Table 1, number 072805). Although these two ages do not overlap as much as our other samples, we are confident that both localities represent the same terrace based on their distribution (Figure 4) and their geomorphic character in the field. The overlap in ages suggests that the T2 surface was abandoned before the time period 30–37 ka, giving a weighted mean age of 34 ± 3 ka (representing 1σ uncertainty).

3.4. Terrace Correlation

Terrace correlation is a critical issue in the study of terrace formation [*Merritts et al.*, 1994]; ensuring that geographically separated treads represent the same fluvial episode can be challenging. In our study, terraces span a streamwise distance of ~20 km along the Jinta River (Figure 8), and the degree of preservation is quite good, particularly for the T4 terrace (Figure 4). In addition to the visual correlation in the field and continuity of the surface, there is a systematic and well-established correlation between

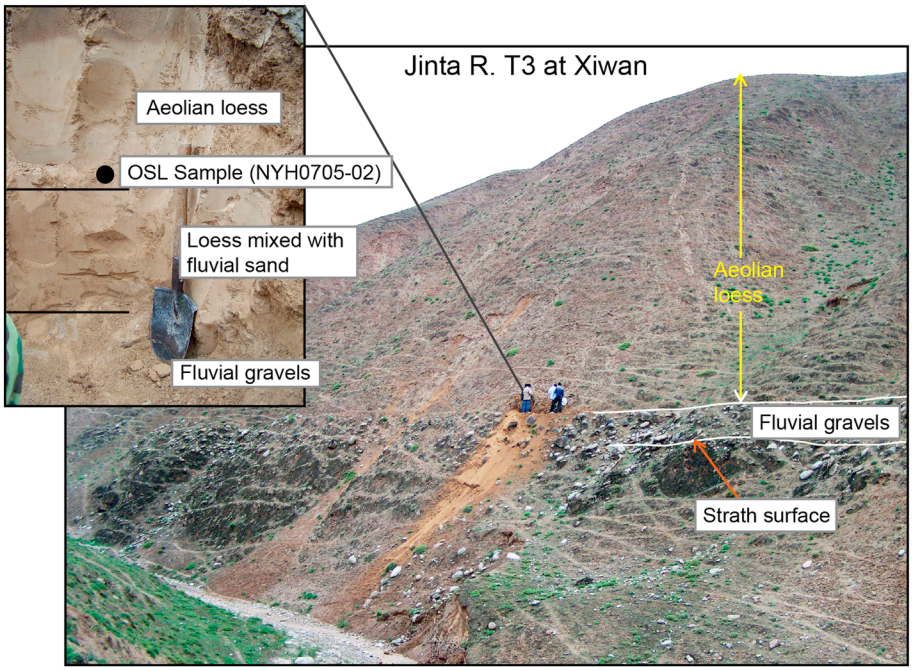

Figure 6. Photos showing the loess covered on fluvial terrace of T3 at Xiwan (Figure 6) and OSL sampling at the base of aeolian loess. Fluvial gravels are capped by a thin layer (~0.5 m) of mixed aeolian loess and fluvial sands and overlain by 25–30 m of aeolian loess.

the depth of loess and terrace age [*Pan et al.*, 2013] that helps guide correlation. Along the Jinta River, the T2 surface is easy to recognize as it sits relatively close to the river, is buried by only thin aeolian loess, and is continuous along the river. The T4 surface is the most areally extensive terrace, and it has a relatively wide tread (Figure 4). Collectively, these properties allow reasonable confidence in our correlations (Figure 8). As discussed further below, our surveys reveal that terraces are deformed across the Nanying anticline from Zuizikou to Nanyingand and displaced across faults F1 and F2 (Figures 8b and 8c).

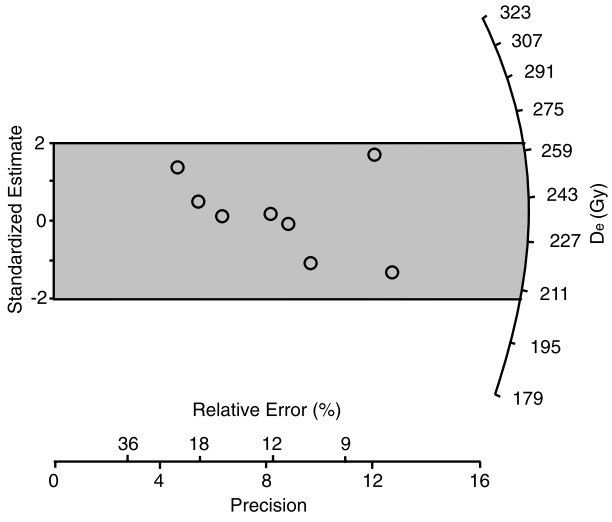

Figure 7. The radial plot of D_e values for the sample 080804 (Table 1). Note that all the D_e values are concentrated without poorly blenched grains.

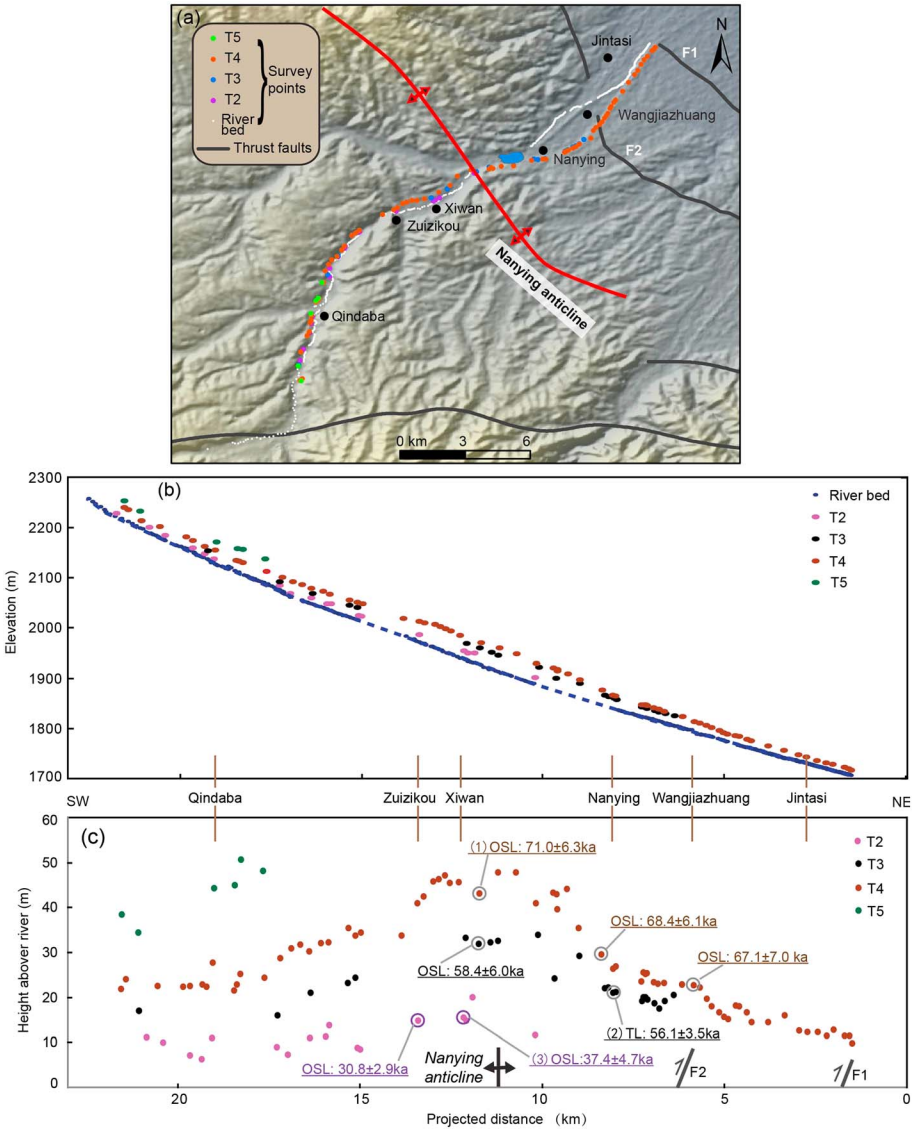

Figure 8. (a) Survey points by differential GPS on terraces and river bed along the Jinta River. (b) Survey results showing the longitudinal profiles of terraces and modern river bed. The vertical exaggeration is 15. (c) Relative heights of the terraces to the modern river bed. The vertical exaggeration is 130. The distance is projected to a vertical plane trending N35°W, parallel with F1 trending. Some of the terrace ages are referenced to (1) [*Pan et al.*, 2013], (2) [*Pan et al.*, 2007], and (3) [*Pan et al.*, 2013], which are also stated in Table 1.

4. Kinematics of Subsurface Thrusting

4.1. Geometry

Our survey results suggest that all three terrace surfaces are deformed across the Nanying anticline (Figures 8 and 9). From the long profiles of the terrace surfaces (Figure 9a), we observe that the fold has several characteristics: (1) it has a relatively short forelimb (~2.3 km), a subhorizontal axial top (~3.4 km), and a relatively long backlimb (~4.6 km); (2) the positions of hinges appear to be similar on the three flights of terraces, suggesting that these hinges have not migrated too much during fold development; (3) the magnitude of deformation across the fold appears to be systematic, increasing with terrace age; and (4) the anticline has a relatively broad wavelength (about 10 km). In addition, terrace surfaces appear to be displaced across faults at the mountain front.

The wavelength of the fold is consistent with previous studies [*Gaudemer et al.*, 1995; *Hou et al.*, 1999] that suggest that folding is associated with slip on a thrust fault at depth. The position of the fault system at

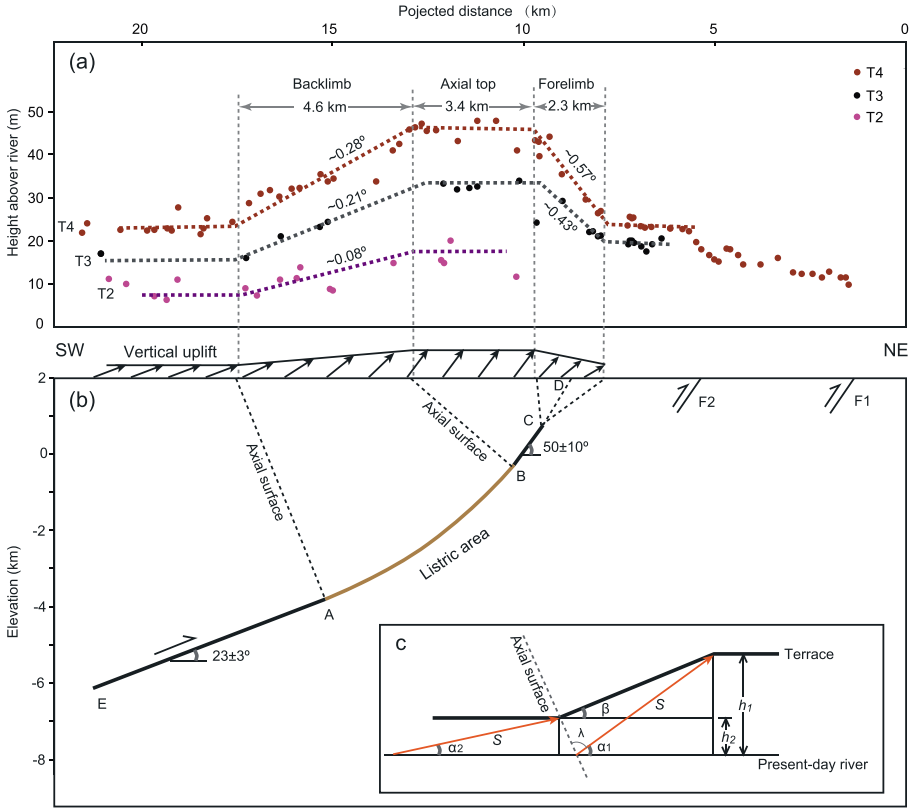

Figure 9. (a) Folded terraces with constant axial surfaces shown by dashed grey lines. (b) Deduced fault geometry by the geometry of folded terraces. Along the blind fault, EA segment has a gentle dip angle, AB is a listric segment, and segment BC has a steep dip angle. The point D represents the intersection of the projection of the fault from C to the surface. (c) Inset shows the relationship of terrace heights and fault dip angles to the amount of fault slip. With the same slip rate (S) along the fault, the terrace height (h_2) is relatively low underlain by a gentle fault dip (α_2), and terrace height (h_1) is relatively high underlain by a steep fault dip (α_1).

the base of a bedrock-cored range and the geometry of the fold do not suggest detachment in a subhorizontal stratum [e.g., *Hubert-Ferrari et al.*, 2007], and so we do not consider this model viable. Along the ~2.3 km long forelimb, the terrace height decreases gradually downstream, indicating that the offset of terrace surface is not associated with a surface-breaking structure. Rather, we infer that the fold is caused by slip along a blind thrust fault [*Burbank and Anderson*, 2012]. Our reconstruction of terrace deformation and fault geometry assumes that individual terrace levels are isochronous markers, that the terrace tread was initially parallel to the modern longitudinal profile, and that bed length and thickness of the fold are preserved. We reconstruct vertical deformation and horizontal distances across different parts of the fold (Figure 9a) and attempt to test various fault geometries to explore which best explains fold geometry (Figure 10).

Models of simple fault-bend folds (Figure 10a) tend to generate short backlimbs and rapid fold growth, as the horizontal width of the backlimb depends on the magnitude of horizontal slip along the fault since the terrace is formed and the dip angle of the backlimb is between the dip angles of the two segments of the fault [*Thompson et al.*, 2002]. Along the Nanying anticline, the backlimb is ~4.6 km and the terrace age is ~70 ka, which means that the fault would slip at a rate of ~70 mm/a for a fault-bend fold. The dip angle of the terrace backlimb along the Nanying anticline is less than 1° (Figure 9a), which is not in agreement with the fault-bend fold geometry [*Thompson et al.*, 2002]. These two facts suggest that the simple fault-bend fold does not fit with our observation. Similarly, with a fault-propagation fold [*Suppe and Medwedeff*, 1990] or a displacement-gradient fold [*Wickham*, 1995], the terrace along the backlimb would have a steep dip angle and short limb length, which will not fit observations along the Nanying anticline.

Along the T4 terrace backlimb, the terrace height gradually increases from ~23 m to ~47 m over a distance of ~4.6 km. Such a low magnitude of vertical rock motion over a long distance suggests a listric

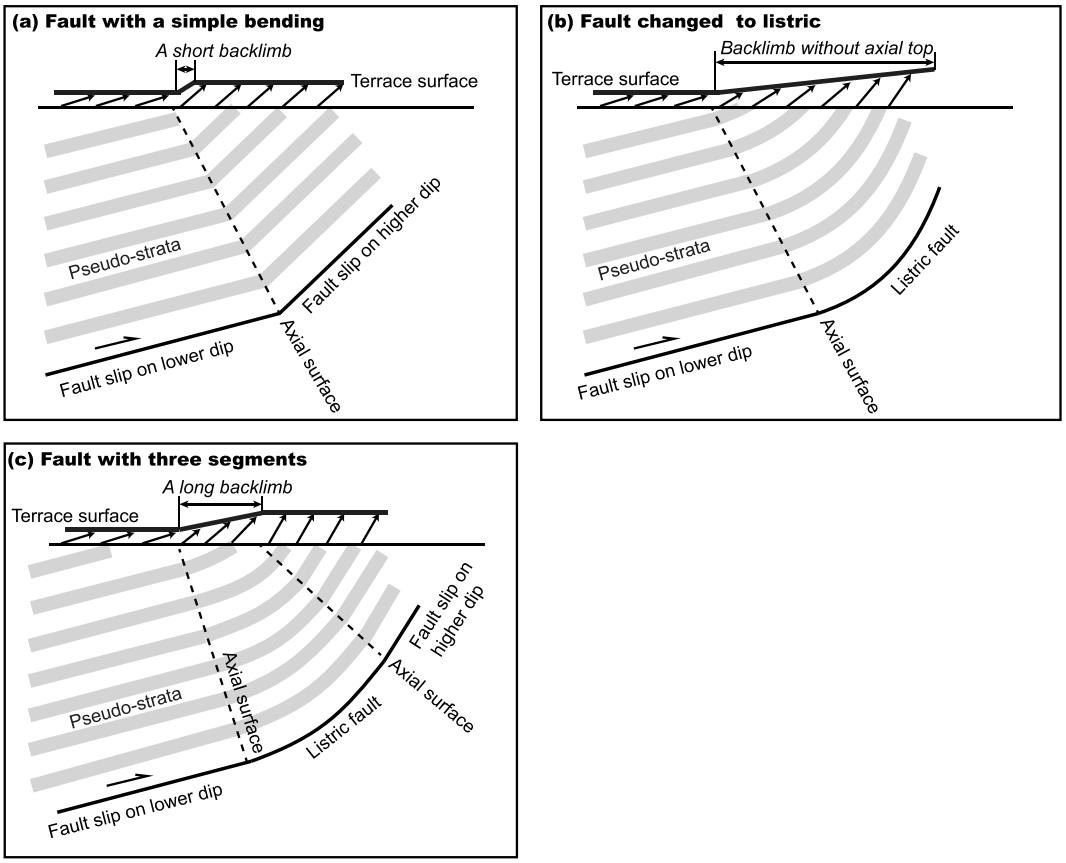

Figure 10. Different models of fault geometry and related terrace deformation. (a) A simple fault-bend fold with a short backlimb on the terrace. (b) The model of a listric fault induced a continues growing backlimb. (c) A fault-bend fold with a listric segment or a wide hinge zone, which induces a relatively long backlimb on the terrace.

fault geometry [*Amos et al*., 2007] or a broad hinge zone [*Suppe et al*., 1997; *Hubert-Ferrari et al*., 2007], both of which will drive a gradual increase in the rate of vertical motion (Figures 10b and 10c). If we assume that the lower portion of the fault remains listric until the fault tip (Figure 10b), the height of the terrace surface can be reasonably fit with the long backlimb, but the model does not explain the flat axial top. A flat axial top at the anticline axis implies that the dip of the thrust fault becomes more linear at shallow depth (Figure 10c). The relatively short forelimb and the slight apparent rotation between the T3 and T4 treads appear to be consistent with displacement-gradient fold theory [*Wickham*, 1995] or a trisher zone [*Erslev*, 1991] such that the continuing displacement along the ramp above the fault tip is accommodated by a decreasing velocity field of vertical uplift (Figure 9). To the north, the décollement may extend continuously between the other two frontal thrust faults F1 and F2 (Figure 9b) of the KNQ thrust system (Figure 2).

The general structure of the blind thrust fault—which it is composed by three segments of fault with different dip angles—allows us to estimate the fault depth using the geometry of the terrace surface. In eastern Qilian Shan, poor exposure of the fault surface prevents a direct determination of fault dip, although previous workers consider the fault to dip between 45 and 52° [*Institute of Geology and Lanzhou Institute of Earthquake* (*China Earthquake Administration*), 1993]. Farther west, the frontal thrust in eastern Qilian Shan is assumed to have a dip angle between 40 and 60° [*Champagnac et al*., 2010; *Gaudemer et al*., 1995], similar to the values assumed for the NFT in the central and western Qilian Shan [*Meyer et al*., 1998; *Hetzel et al*., 2004]. Following these previous studies, we assume that the blind fault tip beneath our study area dips 50 ± 10° (Figure 9). If we assume that the terrace height at terrace formation was parallel to modern river height, the different terrace height along the fold was primarily caused by the fault slip on different dip angle. We calculate the dip angle along the fault behind the

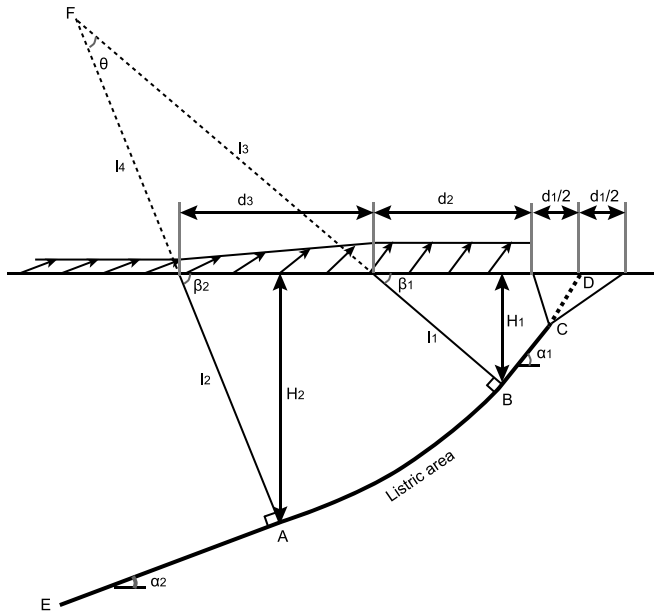

Figure 11. The geometry of underlying thrust fault across the Jinta anticline. d_1: the distance of forelimb, for calculating the fault depth, we simply assume that the fault extrapolation to the surface is the middle of the forelimb; d_2: the distance of the anticline axis; d_3: the distance of backlimb; H_1: the depth of the fault where the listric area end; H_2: the depth of the fault where the listric area begin; l_1 and l_2: the distances of axial surface from the surface to the fault; l_3 and l_4: the distances of the axial surface from the surface to the circle dot, which is the circle dot of the arc for listric area; and α_1 and α_2: the dip angle at shallow fault and at deep fault.

back limb (EA in Figure 11) with the known dip at BC (Figure 11). Following *Thompson et al.* [2002], we assume uniform slip rate along the fault such that (Figure 9c)

$$h_1/\sin\alpha_1 = h_2/\sin\alpha_2, \tag{1}$$

where h_1 is the terrace height on fault ramp with high dip angle α_1 and h_2 is the terrace height on fault ramp with low dip α_2 (Figure 9c). While the difference of heights along a same terrace is primarily caused by the difference in fault dip, the ratio of h_1/h_2 would be the same along different terraces. With our terrace heights of T4, T3, and T2 (Figure 9a), the calculated height ratios are 2.0 ± 0.1, 2.0 ± 0.1, and 2.0 ± 0.4 respectively. The good agreement of the ratios in the three separate terrace treads supports our assumption of the fold geometry. Using the formula (1), the calculated dip angle α_2 along EA (Figure 9) is $23 \pm 3°$, with which the uncertainties are derived from terrace heights and the dip angle of α_1.

Based on the geometry of folded terraces and subsurface fault geometry, we calculate the depths of the inflection points that mark changes in fault dip, from the estimated dip angles and the lengths of the fold limbs (Figure 11). The depth of point B (Figure 11) below the surface, where the listric fault segment changes to a steeper fault near the surface, can be calculated as

$$H_1 = (d_1/2 + d_2)\times\sin\alpha_1\times\cos\alpha_1. \tag{2}$$

The depth of point A (Figure 11), where the thrust fault becomes listric, can be calculated as

$$H_2 = \left[(d_1/2 + d_2)\times\sin\alpha_1 + \frac{d_3}{\sin(\alpha_1 - \alpha_2)}\times(\cos\alpha_2 - \cos\alpha_1)\right]\times\cos\alpha_2. \tag{3}$$

In calculation of the fault depth, we simply use the terrace height of T4, for the T4 has relatively continuous height data and good age control. Depth uncertainties are derived from distances of fold limbs and dip angle of α_1 and α_2. Below the surface, the blind thrust fault geometry from deep to surface is determined as follows: (1) a décollement with dip angle of $23 \pm 3°$ that begins to curve into a listric fault at a depth of 5.8 ± 1.1 km, (2) between 5.8 ± 1.1 km and 2.2 ± 0.1 km depth the fault systematically increases dip to $50 \pm 10°$, and (3) the fault maintains this dip ($50 \pm 10°$) until the fault tip.

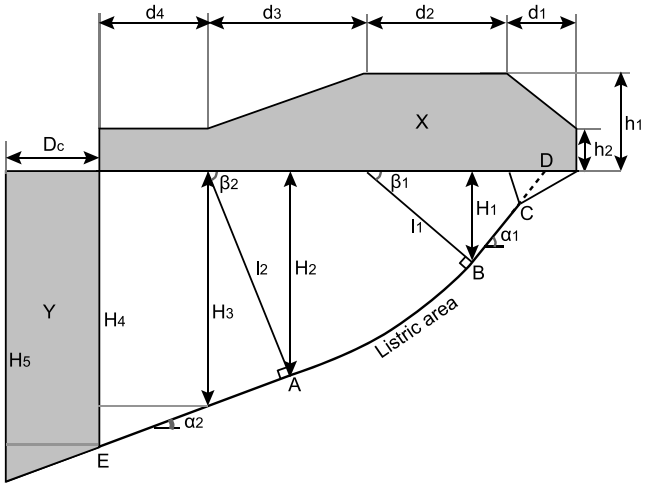

Figure 12. Fault geometry for crust shortening calculation. New value of d_4 is the distance from the backlimb to a certain point in the upstream; H_3, H_4, and H_5 are the depths of the fault for calculating the crust shortening; D_c is the shortening distance since T4 abandonment; X is the uplifted area in the surface, and Y is the shortening area in the crust; and h_1 and h_2 are the terrace heights of T4 at the anticline axis and at north of the forelimb, respectively.

4.2. Deformation Rate

We determine the fault slip rate from the deformed terrace heights and their ages (Figure 8). The relative lower terrace height (Figure 9a) in the upstream of the anticline backlimb is related to the lower dip angle of the thrust along EA (Figure 9b), while the higher terrace height at the anticline hinge area (Figure 9a) is related to the steeper dip angle of the thrust along BC (Figure 9b). The amount of fault slip (S) can be calculated as (Figure 9c)

$$S = \frac{h_1 - h_2}{\sin\alpha_1 - \sin a_2}. \tag{4}$$

This formula is similar to the calculation of fault slip in a fault-bend-related fold [*Thompson et al.*, 2002]. In calculating the fault slip with this formula, we simply assume that the apparent deformation of the terrace surface was purely caused by fold growth. Using the age of terrace abandonment T and determined fault slip amount S, the slip rate R_s of the blind fault can be calculated by $R_s = S/T$. The differences in terrace height ($h_1 - h_2$) of 23 ± 5 m (T4), 17 ± 2 m (T3), and 7 ± 5 m (T2) (Figure 9a) imply corresponding slip rates of 0.9 ± 0.2 mm/a since abandonment of T4 (69 ± 4 ka B.P.), 0.8 ± 0.1 mm/a since abandonment of T3 (57 ± 4 ka B.P.), and 0.5 ± 0.4 mm/a since abandonment of T2 (34 ± 3 ka B.P.). Accounting for uncertainties associated with terrace elevations, fault dips, and terrace ages, it seems likely that fault slip has been relatively constant at ~0.9 mm/a from ~70 ka B.P. to present.

Assuming that area is conserved, we can estimate that the amount of crustal shortening, Y, is equal to surface uplift area X. (Figure 12). We consider uncertainties arising from river accumulation or erosion. Along the Jinta River, the fluvial gravel thickness in terraces is 1–5 m, so we add 5 m uncertainty of terrace height in calculating the uplift mass area X (Figure 12):

$$X = (d_1 + d_2 + d_3 + d_4) \times h_2 + d_2 \times (h_1 - h_2) + (d_1 + d_3) \times \frac{h_1 - h_2}{2} \pm 5 \times (d_1 + d_2 + d_3 + d_4). \tag{5}$$

The shortening area can be calculated as

$$Y = D_c^2 \times \frac{\tan\alpha_2}{2} + (H_3 + d_4 \times \tan\alpha_2) \times D_c. \tag{6}$$

After solution of equations (5) and (6), and using the height data of T4, the shortening since T4 abandonment is determined as 57.9 ± 8.7 m. This yields a shortening rate of 0.8 ± 0.1 mm/a, and the consistency of this calculation with the result (0.8 ± 0.2 mm/a) using fault slip rate indicates that our estimation of crust shortening across the Nanying fold is reliable.

In addition to deformation along the Nanying anticline, the T4 terrace is displaced by fault F2 (Figure 9) and may be displaced by F1 along the mountain front (Figure 2). The offset of T4 tread by F2 is ~9 m (Figure 9a). Assuming a fault dip as $50 \pm 10°$ [*Champagnac et al.*, 2010; *Gaudemer et al.*, 1995] along F2, the fault slip rate along the décollement under F2 would be 0.2 ± 0.1 mm/a and yields a shortening rate of 0.1 ± 0.1 mm/a. Thus, the total crustal shortening rate is about 0.9 ± 0.3 mm/a from the H-T fault to the KNQ fault.

5. Discussion

In our study area, active deformation is driven by slip along the underlying thrust (Figure 9) between the H-T fault and the KNQ fault (Figure 2). Deformation along the Nanying anticline is appears to have been

continuous over the past circa 70 ka, and the subsurface fault architecture (Figure 9) is in general agreement with the structure proposed by *Gaudemer et al*. [1995], but with a somewhat shallower depth. Between the H-T fault and KNQ fault (Figure 2), the slip rate of 0.9 ± 0.2 mm/a along the blind fault since ~70 ka B.P. is of the same magnitude as 0.5–1.0 mm/a of fault slip in the middle portion of the Qilian Shan [*Hetzel et al*., 2004; *Zheng et al*., 2010] and 0.5–0.8 mm/a of mountain uplift along the Yumu Shan [*Palumbo et al*., 2009], suggesting that the frontal fault system along the Qilian Shan exhibits generally similar rates of shortening along much of its length. The exception to this occurs along the Fengle fault near the Xiying River, where Champagnac and co-authors determined a slip rate of 2.8 ± 1.3 mm/a [*Champagnac et al*., 2010]. Summing the slip rate on the F1 fault with the slip rate underlying the Nanying anticline, the total slip rate along the décollement would be ~1.1 mm/a, still lower than the minimum bound of the slip rate estimated along the Fengle fault. The relatively high slip rate may be derived from uncertainties in fault offset estimation as discussed by *Hetzel* [2013] and from uncertainties in age control, perhaps related to the presence/absence of loess cover at each site. Until more complete records of slip through time are developed, we are unable to assess the case of these differences.

Modern shortening rates across the eastern Qilian Shan, as measured by GPS surveys, are ~5 mm/a in a NE-SW direction and spanning a distance of >200 km from the Riyueshan Fault in the south to the Hexi Corridor in the north [*Zheng et al*., 2013b]. Our determination of a shortening rate of 0.9 ± 0.3 mm/a across the northern frontal thrust system (the KNQ fault) suggests that the crustal shortening across the NE Tibetan Plateau is not entirely accomplished along the frontal thrust but must be distributed along several thrust and fold systems. To the south of the KNQ fault system, shortening along the H-T fault [*Gaudemer et al*., 1995], lateral slip along the Haiyuan Fault [*Lasserre et al*., 2002], and deformation along subsidary fault-fold systems south of the Haiyuan Fault [*Yuan et al*., 2013] presumably accommodate the remaining ~75% of the crustal shortening. The GPS velocity data across the Qilian Shan [*Zhang et al*., 2004; *Zheng et al*., 2013b] also show a gradually decreasing pattern from south to north, which supports an argument of distributed crustal shortening on several fault systems [*Hetzel et al*., 2004]. To the north of the H-T fault, the ~1.1 mm/a slip rate (or ~0.9 mm/a shortening) along the base thrust (the décollement) may suggest a relatively long time interval of great earthquake hazard in the eastern Qilian Shan region. The Gulang 1927 $M = 8$–8.3 earthquake occurred along the southern, deep portion of the basal thrust [*Gaudemer et al*., 1995]. Our results suggest that slip rate along this portion of the fault system must be at least ~1.2 mm/a and could be higher given that shortening along the H-T fault must add into the system. Unfortunately, reliable long-term slip rates are as yet unknown along the H-T fault. The surface rupture during the 1927 Gulang earthquake exhibited vertical displacement of 2.5–3.5 m [*Hou*, 1998], and this amount of slip suggests that similar magnitude earthquakes could occur every 2000–3000 years.

In eastern Qilian Shan, a significant fraction of the total crustal shortening is accommodated by folding in the mountain range (Figure 2). Thus, our results provide an example where not all deformation is accomplished along the range-bounding faults, such as the NFT [*Champagnac et al*., 2010; *Hetzel*, 2013; *Tapponnier et al*., 1990; *Zheng et al*., 2010]. In our investigations, if we were to simply calculate the shortening along scarps preserved at the mountain front (F1 and F2 in Figure 9), we would greatly underestimate the rate of shortening along the region. These results suggest that continuous deformation of the mountain range is primarily related to long-term slip along a blind thrust growing from the décollement. In this context, the mountain front faults are relatively new and accomplish little of the total displacement. Thus, our results suggest that distributed folding may be underappreciated in active ranges where a lack of preserved markers, such as fluvial terraces, hinders reconstruction of distributed deformation and folding.

6. Conclusions

In mountainous regions, folded fluvial terraces provide markers from which to reconstruct the geometries and rates of deformation along subsurface fault systems. In the eastern Qilian Shan, the Nanying anticline is related to a blind thrust fault with the geometry that a listric area is placed between two portions of dip slip with different angle, which induces the differences of vertical deformation of the terrace surfaces. In the eastern Qilian Shan, surface deformation associated with fault-related folding is an important process in accommodating crustal shortening associated with growth of the range.

Acknowledgments
The data used in this study are available upon request from the authors. This work was financially supported by the National Natural Science Foundation of China (NSFC) project 41471009, the Key Project of the Major Research Plan of the NSFC 91125008, and NSFC project 41001003. The first author also thanks China Scholarship Council (CSC) for supporting his visit to Oregon State University for collaborative research. We further thank J.F. Chen, N.N. Chu, X.L. Wang, S.F. Jiang, J. Wang, and C. Zhang for their assistance with field work. Y.X. Fan, T.L. Fan, and D.F Mu assisted with analysis with OSL data. We thank A. Densmore for comments on a previous version of this manuscript and two anonymous reviewers for their valuable suggestions on the present version.

References

Aitken, M. J. (1998), *An Introduction to Optical Dating: The Dating of Quaternary Sediments by the Use of Photon-Stimulated Luminescence*, Oxford Univ. Press on Demand, Oxford.

Allmendinger, R. W. (1998), Inverse and forward numerical modeling of trishear fault-propagation folds, *Tectonics*, *17*(4), 640–656, doi:10.1029/98TC01907.

Amos, C. B., D. W. Burbank, D. C. Nobes, and S. A. L. Read (2007), Geomorphic constraints on listric thrust faulting: Implications for active deformation in the Mackenzie Basin, South Island, New Zealand, *J. Geophys. Res.*, *112*, B03S11, doi:10.1029/2006JB004291.

Banerjee, D., A. S. Murray, L. Bøtter-Jensen, and A. Lang (2001), Equivalent dose estimation using a single aliquot of polymineral fine grains, *Radiat. Meas.*, *33*(1), 73–94, doi:10.1016/S1350-4487(00)00101-3.

Benedetti, L., P. Tapponnier, G. C. P. King, B. Meyer, and I. Manighetti (2000), Growth folding and active thrusting in the Montello region, Veneto, northern Italy, *J. Geophys. Res.*, *105*(B1), 739–766, doi:10.1029/1999JB900222.

Burbank, D. W., and R. S. Anderson (2012), *Tectonic Geomorphology*, 2nd ed., pp. 107–112, John Wiley, Oxford, U. K.

Burchfiel, B. C., Q. Deng, P. Molnar, L. Royden, Y. Wang, P. Zhang, and W. Zhang (1989), Intracrustal detachment within zones of continental deformation, *Geology*, *17*(8), 748–752.

Burchfiel, B. C., E. T. Brown, D. Qidong, F. Xianyue, L. Jun, P. Molnar, S. Jianbang, W. Zhangming, and Y. Huichuan (1999), Crustal shortening on the margins of the Tien Shan, Xinjiang, China, *Int. Geol. Rev.*, *41*(8), 665–700, doi:10.1080/00206819909465164.

Champagnac, J. D., D. Y. Yuan, W. P. Ge, P. Molnar, and W. J. Zheng (2010), Slip rate at the north-eastern front of the Qilian Shan, China, *Terra Nova*, *22*(3), 180–187, doi:10.1111/j.1365-3121.2010.00932.x.

Chen, J., R. Heermance, D. W. Burbank, K. M. Scharer, J. J. Miao, and C. S. Wang (2007), Quantification of growth and lateral propagation of the Kashi anticline, southwest Chinese Tian Shan, *J. Geophys. Res.*, *112*, B03S16, doi:10.1029/2006JB004345.

Chen, W. B. (2003), Principal features of tectonic deformation and their generation mechanism in the Hexi Corridor and its adjacent regions since Late Quaternary [in Chinese], PhD thesis, pp. 32–55, Institute of Geology, China Seismological Bureau, Beijing.

Daëron, M., J. P. Avouac, and J. Charreau (2007), Modeling the shortening history of a fault tip fold using structural and geomorphic records of deformation, *J. Geophys. Res.*, *112*, B03S13, doi:10.1029/2006JB004460.

Erslev, E. A. (1991), Trishear fault-propagation folding, *Geology*, *19*(6), 617–620, doi:10.1130/0091-7613(1991)019<0617:tfpf>2.3.co;2.

Fan, Y. X., H. Zhao, and F. H. Chen (2010), The equivalent dose of different grain size quartz fractions from lakeshore sediments in the arid region of north China, *Quat. Geochronol.*, *5*(2), 205–211, doi:10.1016/j.quageo.2009.05.012.

Fan, Y., X. Chen, W. Liu, F. Zhang, and F. Zhang (2015), Formation of present desert landscape surrounding Jilantai Salt Lake in northern China based on OSL dating, *Front. Earth Sci.*, *9*(3), 497–508, doi:10.1007/s11707-014-0482-3.

Fang, X. M., Z. J. Zhao, J. J. Li, M. D. Yan, and B. T. Pan (2005), Magnetostratigraphy of the late Cenozoic Laojunmiao anticline in the northern Qilian Mountains and its implications for the northern Tibetan Plateau uplift, *Sci. China Ser. D*, *48*(7), 1040–1051, doi:10.1360/03yd0188.

Gansu Geological Bureau (1989), *Regional Geology of Gansu Province* [in Chinese], 692 p., Geological Publishing House, Beijing.

Gaudemer, Y., P. Tapponnier, B. Meyer, G. Peltzer, G. Shunmin, and Z. T. Chen (1995), Partitioning of crustal slip between linked, active faults in the eastern Qilian Shan, and evidence for a major seismic gap, the "Tianzhu gap", on the western Haiyuan Fault, Gansu (China), *Geophys. J. Int.*, *120*, 599–645, doi:10.1111/j.1365-246X.1995.tb01842.x.

Geoge, A. D., S. J. Marshallsea, K.-H. Wyrwoll, J. Chen, and Y. Lu (2001), Miocene cooling in the northern Qilian Shan, northeastern margin of the Tibetan Plateau, revealed by apatite fission-track and vitrinite-reflectance analysis, *Geology*, *29*(10), 939–942, doi:10.1130/0091-7613(2001)029<0939:MCITNQ>2.0.CO;2.

Gold, R. D., E. Cowgill, X.-F. Wang, and X.-H. Chen (2006), Application of trishear fault-propagation folding to active reverse faults: Examples from the Dalong Fault, Gansu Province, NW China, *J. Struct. Geol.*, *28*(2), 200–219, doi:10.1016/j.jsg.2005.10.006.

Hardy, S., and J. Poblet (1994), Geometric and numerical model of progressive limb rotation in detachment folds, *Geology*, *22*(4), 371–374, doi:10.1130/0091-7613(1994)022<0371:ganmop>2.3.co;2.

Hetzel, R. (2013), Active faulting, mountain growth, and erosion at the margins of the Tibetan Plateau constrained by in situ-produced cosmogenic nuclides, *Tectonophysics*, *582*, 1–24, doi:10.1016/j.tecto.2012.10.027.

Hetzel, R., S. Niedermann, M.-X. Tao, P. W. Kubik, S. Ivy-Ochs, B. Gao, and M. R. Strecker (2002), Low slip rates and long-term preservation of geomorphic features in Central Asia, *Nature*, *417*, 428–432, doi:10.1038/417428a.

Hetzel, R., M. Tao, S. Stokes, S. Niedermann, S. Ivy-Ochs, B. Gao, M. R. Strecker, and P. W. Kubik (2004), Late Pleistocene/Holocene slip rate of the Zhangye thrust (Qilian Shan, China) and implications for the active growth of the northeastern Tibetan Plateau, *Tectonics*, *23*, TC6006, doi:10.1029/2004TC001653.

Hetzel, R., S. Niedermann, M. Tao, P. W. Kubik, and M. R. Strecker (2006), Climatic versus tectonic control on river incision at the margin of NE Tibet: ^{10}Be exposure dating of river terraces at the mountain front of the Qilian Shan, *J. Geophys. Res.*, *111*, F03012, doi:10.1029/2005JF000352.

Hou, K. (1998), Characteristics of ground ruptures caused by 1927 Gulang M8 earthquake and their causative mechanisms [in Chinese with English abstract], *Seismol. Geol.*, *20*(1), 19–26.

Hou, K., Q. Deng, and B. Liu (1999), Research on tectonic environment and seismogenic mechanism of 1927 Gulang great earthquake [in Chinese with English abstract]. *Earthquake Res. China*, *15*(4), 339–348.

Hu, X. F., E. Kirby, B. T. Pan, D. E. Granger, and H. Su (2011), Cosmogenic burial ages reveal sediment reservoir dynamics along the Yellow River, China, *Geology*, *39*(9), 839–842, doi:10.1130/G32030.1.

Hubert-Ferrari, A., J. Suppe, R. Gonzalez-Mieres, and X. Wang (2007), Mechanisms of active folding of the landscape (southern Tian Shan, China), *J. Geophys. Res.*, *112*, B03S09, doi:10.1029/2006JB004362.

Institute of Geology and Lanzhou Institute of Earthquake (China Earthquake Administration) (1993), *Active Fault Systems in the Qilian Mountain-Hexi Corridor* [in Chinese], p. 93, Seismological Press, Beijing.

Lasserre, C., Y. Gaudemer, P. Tapponnier, A. S. Meriaux, J. Van der Woerd, D. Y. Yuan, F. J. Ryerson, R. C. Finkel, and M. W. Caffee (2002), Fast late Pleistocene slip rate on the Leng Long Ling segment of the Haiyuan Fault, Qinghai, China, *J. Geophys. Res.*, *107*(B11), 2276, doi:10.1029/2000JB000060.

Lavé, J., and J. P. Avouac (2000), Active folding of fluvial terraces across the Siwaliks Hills, Himalayas of central Nepal, *J. Geophys. Res.*, *105*(B3), 5735–5770, doi:10.1029/1999JB900292.

Liu, D. L., M. D. Yan, X. M. Fang, H. B. Li, C. H. Song, and S. Dai (2011), Magnetostratigraphy of sediments from the Yumu Shan, Hexi Corridor and its implications regarding the Late Cenozoic uplift of the NE Tibetan Plateau, *Quat. Int.*, *236*(1–2), 13–20, doi:10.1016/j.quaint.2010.12.007.

Merritts, D. J., K. R. Vincent, and E. E. Wohl (1994), Long river profiles, tectonism, and eustasy: A guide to interpreting fluvial terraces, *J. Geophys. Res.*, *99*(B7), 14,031–14,050, doi:10.1029/94JB00857.

Meyer, B., P. Tapponnier, L. Bourjot, F. Metivier, Y. Gaudemer, G. Peltzer, S. Guo, and Z. Chen (1998), Crustal thickening in Gansu-Qinghai, lithospheric mantle subduction, and oblique, strike-slip controlled growth of the Tibet plateau, *Geophys. J. Int.*, *135*(1), 1–47, doi:10.1046/j.1365-246X.1998.00567.x.

Molnar, P., E. T. Brown, B. C. Burchfiel, Q. Deng, X. Feng, J. Li, and G. M. Raisbeck (1994), Quaternary climate change and the formation of river terraces across growing anticlines on the north flank of the Tien Shan, China, *J. Geol.*, *102*, 583–602.

Palumbo, L., R. Hetzel, M. X. Tao, X. B. Li, and J. M. Guo (2009), Deciphering the rate of mountain growth during topographic presteady state: An example from the NE margin of the Tibetan Plateau, *Tectonics*, *28*, TC4017, doi:10.1029/2009TC002455.

Pan, B. T., D. Burbank, Y. X. Wang, G. J. Wu, J. J. Li, and Q. Y. Guan (2003), A 900 ky record of strath terrace formation during glacial-interglacial transitions in northwest China, *Geology*, *31*(11), 957–960, doi:10.1130/G19685.1.

Pan B. T., H. S. Gao, B. Y. Yuan, and J. J. Li (2004), Step-like landforms and uplift of the Qinghai-Xizang Plateau [in Chinese with English abstract], *Qut. Sci.*, *24*(1), 50–57.

Pan, B. T., H. S. Gao, G. J. Wu, J. J. Li, B. Y. Li, and Y. G. Ye (2007), Dating of erosion surface and terraces in the eastern Qilian Shan, northwest China, *Earth Surf. Proc. Landforms*, *32*(1), 143–154, doi:10.1002/esp.1390.

Pan, B. T., X. F. Hu, H. S. Gao, Z. B. Hu, B. Cao, H. P. Geng, and Q. Y. Li (2013), Late Quaternary river incision rates and rock uplift pattern of the eastern Qilian Shan Mountain, China, *Geomorphology*, *184*, 84–97, doi:10.1016/j.geomorph.2012.11.020.

Rockwell, T. K., E. A. Keller, and G. R. Dembroff (1988), Quaternary rate of folding of the Ventura Avenue anticline, western Transverse Ranges, southern California, *Geol. Soc. Am. Bull.*, *100*(6), 850–858, doi:10.1130/0016-7606(1988)100<0850:qrofot>2.3.co;2.

Scharer, K. M., D. W. Burbank, J. Chen, and R. J. Weldon (2006), Kinematic models of fluvial terraces over active detachment folds: Constraints on the growth mechanism of the Kashi-Atushi fold system, Chinese Tian Shan, *Geol. Soc. Am. Bull.*, *118*(7–8), 1006–1021, doi:10.1130/B25835.1.

Storti, F., and J. Poblet (1997), Growth stratal architectures associated to decollement folds and fault-propagation folds. Inferences on fold kinematics, *Tectonophysics*, *282*(1–4), 353–373, doi:10.1016/S0040-1951(97)00230-8.

Suppe, J. (1983), Geometry and kinematics of fault-bend folding, *Am. J. Sci.*, *283*(7), 684–721, doi:10.2475/ajs.283.7.684.

Suppe, J. (1992), Rates of folding and faulting determined from growth strata, in *Thrust Tectonics*, pp. 105–121, Springer, Netherlands, doi:10.1007/978-94-011-3066-0_9.

Suppe, J., and D. A. Medwedeff (1990), Geometry and kinematics of fault-propagation folding, *Eclogae Geol. Helv.*, *83*, 409–454.

Suppe, J., F. Sàbat, J. A. Muñoz, J. Poblet, E. Roca, and J. Vergés (1997), Bed-by-bed fold growth by kink-band migration: Sant Llorenç de Morunys, eastern Pyrenees, *J. Struct. Geol.*, *19*(3), 443–461, doi:10.1016/S0191-8141(96)00103-4.

Tapponnier, P., et al. (1990), Active thrusting and folding in the Qilian Shan, and decoupling between upper crust and mantle in northeastern Tibet, *Earth Planet. Sci. Lett.*, *97*(3), 382–403, doi:10.1016/0012-821X(90)90053-Z.

Thompson, S. C., R. J. Weldon, C. M. Rubin, K. Abdrakhmatov, P. Molnar, and G. W. Berger (2002), Late Quaternary slip rates across the central Tien Shan, Kyrgyzstan, central Asia, *J. Geophys. Res.*, *107*(B9), 2203, doi:10.1029/2001JB000596.

Wang, Y., B. T. Pan, H. S. Gao, Q. Y. Guan, and J. P. Wang (2007), Magnetic fabric-based reconstruction of the paleowind direction from a loess sequence in the northeastern flank of the Qilian Mountains, *Chin. J. Geophys.*, *50*(4), 1005–1010, doi:10.1002/cjg2.1117.

Wickham, J. (1995), Fault displacement-gradient folds and the structure at Lost Hills, California (U.S.A.), *J. Struct. Geol.*, *17*(9), 1293–1302, doi:10.1016/0191-8141(95)00029-D.

Wilson, L. F., F. J. Pazzaglia, and D. J. Anastasio (2009), A fluvial record of active fault-propagation folding, Salsomaggiore anticline, northern Apennines, Italy, *J. Geophys. Res.*, *114*, B08403, doi:10.1029/2008JB005984.

Wu, G. J., B. T. Pan, J. J. Li, Q. Y. Guan, and Z. G. Liu (2001), Tectonic-climatic events in eastern Qilian Mountains over the past 0.83 Ma, *Sci. China Ser. D*, *44*, 251–260, doi:10.1007/BF02911994.

Yang, S. F., H. L. Chen, X. G. Cheng, A. C. Xiao, J. J. Chen, M. T. Fan, and D. W. Tain (2007), *The Structural Characteristics of Northern Qilian Shan Mountain Thrust Belt and Its Control on the Oil and Gas Accumulation* [in Chinese with English abstract], Science Press, Beijing.

Yuan, D. Y., W. P. Ge, Z. W. Chen, C. Y. Li, Z. C. Wang, H. P. Zhang, P. Z. Zhang, D. W. Zheng, W. J. Zheng, and W. H. Craddock (2013), The growth of northeastern Tibet and its relevance to large-scale continental geodynamics: A review of recent studies, *Tectonics*, *32*, 1358–1370, doi:10.1002/tect.20081.

Zhang, P. Z., Z. K. Shen, W. Min, W. J. Gan, and R. Burgmann (2004), Continuous deformation of the Tibetan Plateau from global positioning system data, *Geology*, *32*(9), 809–812, doi:10.1130/G20554.1.

Zheng, D. W., M. K. Clark, P. Z. Zhang, W. J. Zheng, and K. A. Farley (2010), Erosion, fault initiation and topographic growth of the North Qilian Shan (northern Tibetan Plateau), *Geosphere*, *6*(6), 937–941, doi:10.1130/ges00523.1.

Zheng, W. J., H. P. Zhang, P. Z. Zhang, P. Molnar, X. W. Liu, and D. Y. Yuan (2013a), Late Quaternary slip rates of the thrust faults in western Hexi Corridor (Northern Qilian Shan, China) and their implications for northeastward growth of the Tibetan Plateau, *Geosphere*, *9*(2), 342–354, doi:10.1130/GES00775.1.

Zheng, W. J., P. Z. Zhang, W. G. He, D. Y. Yuan, Y. X. Shao, D. W. Zheng, W. P. Ge, and W. Min (2013b), Transformation of displacement between strike-slip and crustal shortening in the northern margin of the Tibetan Plateau: Evidence from decadal GPS measurements and late Quaternary slip rates on faults, *Tectonophysics*, *584*, 267–280, doi:10.1016/j.tecto.2012.01.006.

Zheng, W. J., P. Z. Zhang, W. P. Ge, P. Molnar, H. P. Zhang, D. Y. Yuan, and J. H. Liu (2013c), Late Quaternary slip rate of the South Heli Shan Fault (northern Hexi Corridor, NW China) and its implications for northeastward growth of the Tibetan Plateau, *Tectonics*, *32*, 271–293, doi:10.1002/TECT.20022.